THE JOURNAL OF PHYSICAL CHEMISTRY C

Article

pubs.acs.org/JPCC

$NaYF_4:Er^{3+},Yb^{3+}/SiO_2$ Core/Shell Upconverting Nanocrystals for Luminescence Thermometry up to 900 K

Robin G. Geitenbeek,*[,†] P. Tim Prins,[†] Wiebke Albrecht,[‡] Alfons van Blaaderen,[‡] Bert M. Weckhuysen,[†] and Andries Meijerink[†]

[†]Department of Chemistry, and [‡]Department of Physics, Debye Institute of Nanomaterials Science, Utrecht University, P.O. Box 80000, 3508TA Utrecht, The Netherlands

Supporting Information

ABSTRACT: The rapid development of nanomaterials with unique size-tunable properties forms the basis for a variety of new applications, including temperature sensing. Luminescent nanoparticles (NPs) have demonstrated potential as sensitive nanothermometers, especially in biological systems. Their small size offers the possibility of mapping temperature profiles with high spatial resolution. The temperature range is however limited, which prevents use in high-temperature applications such as, for example, nanoelectronics, thermal barrier coatings, and chemical reactors. In this work, we extend the temperature range for nanothermometry beyond 900 K using silica-coated $NaYF_4$ nanoparticles doped with the lanthanide ions Yb^{3+} and Er^{3+}. Monodisperse ~20 nm $NaYF_4$:Yb,Er nanocrystals were coated with a ~10 nm silica shell. Upon excitation with infrared radiation, bright green upconversion (UC) emission is observed. From the intensity ratio between $^2H_{11/2}$ and $^4S_{3/2}$ UC emission lines at 520 and 550 nm, respectively, the temperature can be determined up to at least 900 K with an accuracy of 1−5 K for silica-coated NPs. For bare $NaYF_4$:Yb,Er NPs, the particles degrade above 600 K. Repeated thermal cycling experiments demonstrate the high durability and reproducibility of the silica-coated nanocrystals as temperature probes without any loss of performance. The present results open avenues for the development of a new class of highly stable nanoprobes by applying a silica coating around a wide variety of lanthanide-doped NPs.

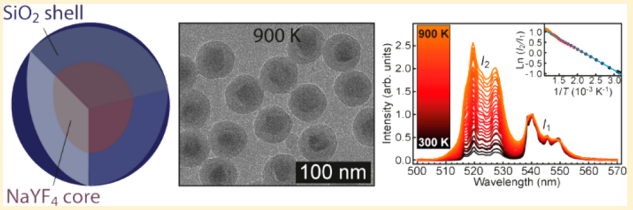

INTRODUCTION

The broad range of potential applications for nanomaterials continues to stimulate research in the nanoregime where size-dependent physical and chemical properties are important in realizing technological breakthroughs.[1−8] One research area involves the development of detection techniques with sufficient spatial resolution enabled by the small size of nanomaterials. Temperature is an important parameter but is not easy to measure with sufficient resolution, that is at the (sub)micrometer scale. In order to measure temperature accurately, several techniques have been developed. These techniques can be divided into three different categories: electrical,[9] mechanical,[10] and optical techniques.[11,12] Most electrical techniques combine the relation between temperature and resistance, voltage, conductivity, or electrical capacity with atomic force microscopy (AFM). Mechanical techniques revolve around an AFM tip composed of two metals and the temperature-dependent contact potential between these metals. Although high resolution can be reached with these techniques, the techniques are limited to surfaces. Furthermore, the techniques require contact with the sample and can therefore initiate artificial heat fluxes.

Optical techniques rely on changes in the absorption or emission spectrum induced by temperature changes and do allow for remote temperature sensing. A promising method is luminescence thermometry.[13,14] Luminescence thermometry exploits the temperature dependence of the spectral position, bandwidth, intensity, polarization, or lifetime of emission. However, most of these optical properties can also depend on other parameters, such as the concentration of luminescent centers, spectral or intensity shifts induced by other factors besides temperature, or fluctuations in the excitation power or spectral alignment. Fluorescence intensity ratio thermometry (FIRT) is a ratiometric measuring technique and consequently does not depend on variations in sample concentration, alignment, or excitation power. This makes FIRT the ideal technique to measure temperature because it does not require an internal standard.

FIRT is an active and expanding field of research. Most of the research presently focuses on in vivo thermometry for bioimaging.[15,16] Research has, for example, shown that FIRT can be applied for cancer diagnosis.[17] In cancer, rapid mitosis leads to increased cell temperatures. These increased cell temperatures can be monitored at an earlier stage than with conventional techniques for cancer diagnosis. The temperature probes should have high accuracy in the physiological range. The range and the accuracy of the temperature measurements cannot be optimized simultaneously. Consequently, the highly

Received: October 11, 2016
Revised: January 12, 2017
Published: January 20, 2017

DOI: 10.1021/acs.jpcc.6b10279
J. Phys. Chem. C 2017, 121, 3503−3510

sensitive temperature probes used for cancer diagnosis have a very limited measuring range (below 350 K).

Many applications, for example, temperature sensing in nanoelectronics,[18,19] nanophotonics,[20,21] thermal barrier coatings,[22,23] and chemical reactors,[24,25] require a much broader temperature range compared to bioimaging. FIRT can be a promising technique in a wider temperature range. However, this requires the temperature probes to be robust and photostable up to elevated temperatures. Ln^{3+}-doped materials are ideal candidates as temperature probes due to their sharp emission lines (easy detection against a broad background), high thermal quenching temperatures of their emission, and high photostability. The Ln^{3+}-doped materials can be organic clusters, metal/organic frameworks, glasses, or (nano)-crystals.[26−29] The use of lanthanides in inorganic hosts is favored over organometallic materials, mostly because of the higher (thermal and photo) stability of the inorganic host and the lower energies of vibrations (phonons) in close proximity to the Ln^{3+} ion. It is well-known that the main mechanism for quenching of the 4f−4f emission of Ln^{3+} is multiphonon relaxation, a process in which energy is transferred from a Ln^{3+} excited state to vibrational excited states (heat) of the surrounding matrix. The relaxation rate depends exponentially on the number of phonons that needs to be excited. As a result, multiphonon relaxation has a much lower probability in inorganic hosts that have low-energy phonons (ca. 600 cm^{-1} for fluorides and oxides) compared to organic materials where large energy gaps can be bridged by a small number of high-energy vibrations (e.g., 3000 and 3500 cm^{-1} for C−H and O−H vibrations, respectively).[30]

On the basis of these advantages, both doped glasses[31,32] and doped crystalline materials[33−35] have been investigated as functional materials for remote temperature sensing using FIRT. However, most of the works focus on bulk materials, with limited spatial resolution and no possibility to measure temperature in stable dispersions. Furthermore, research into both bulk and nanomaterials has led to temperature probes in a range up to 700 K.[32,33,35] However, some applications require much higher temperatures, even up to 1500 K,[36] which cannot be measured with the currently available temperature probes. To measure temperature with sufficient spatial resolution and at elevated temperatures, new temperature (nano)probes need to be developed.

In this work, we report the application of $NaY_{0.8}Yb_{0.18}Er_{0.02}F_4$ nanocrystals (NCs) and $NaY_{0.8}Yb_{0.18}Er_{0.02}F_4/SiO_2$ core/shell ($NaYF_4$@SiO_2) NCs as upconverting (UC) nanothermometers. The monodisperse core nanoparticles show temperature-dependent UC luminescence up to 600 K. The luminescence drops at higher temperatures due to oxidation of the ligands and coalescence of NCs. To overcome this problem, a silica coating has been grown around the core NCs, resulting in core/shell NCs. These $NaYF_4$@SiO_2 NCs show stable temperature-dependent UC luminescence up to 900 K. Repeated cycling between 300 and 900 K shows that the durability of the $NaYF_4$@SiO_2 NCs is excellent. The accuracy of the measurements is also high, with standard deviations of 1 and 5 K below and above 750 K, respectively. The present results show that $NaYF_4$ doped with Yb^{3+} and Er^{3+} can be used as a temperature probe up to 900 K after encapsulation in a protective silica shell. The broader temperature range, the durability of the temperature probes, and the noninvasiveness of FIRT make this system ideal for measuring temperatures in a wide variety of systems and remote temperature sensing applications.

STRUCTURAL CHARACTERIZATION

To determine the size, shape, and crystallinity of both the $NaYF_4$ NCs and $NaYF_4$@SiO_2 NCs, we used different characterization methods such as transmission electron microscopy (TEM), energy dispersive X-ray spectroscopy (EDX), and powder X-ray diffraction (XRD) measurements. Figure 1 shows TEM images of the prepared NCs, and Figure S1 (Supporting Information (SI)) shows the corresponding EDX spectra and XRD diffractograms.

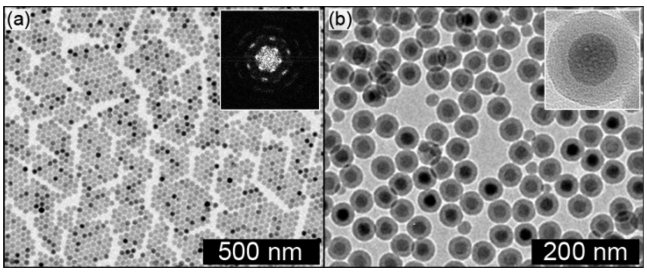

Figure 1. TEM micrographs of the prepared $NaYF_4$ NCs (a, including the inset with a Fourier transform) and $NaYF_4$@SiO_2 NCs (b). The average diameter of the core NCs is 21.7 ± 1.1 nm, and the silica shell is 10.0 ± 0.7 nm.

Figure 1a shows that the synthesis yields monodisperse NCs of 21.7 ± 1.1 nm. The individual NCs are well separated due to the steric effects of the ligand layer, which suggests that the NCs can form a colloidal stable dispersion. These monodisperse NCs form hexagonally ordered domains, which is illustrated with the Fourier transform in the inset. The overgrowth with silica yields monodisperse $NaYF_4$@SiO_2 NCs with an unaltered core and a uniform shell of 10.0 ± 0.7 nm, which are charge stabilized by surface silanol groups.

The elemental composition of the NCs was determined by EDX (Figure S1a,b, SI). From the observed peaks, it can be concluded that Na, Y, F, Er, and Yb are all present in the $NaYF_4$ NCs and $NaYF_4$@SiO_2 NCs. For the $NaYF_4$@SiO_2 NCs, an additional peak for Si is observed along with a strongly increased peak corresponding to O, as expected for silica overgrowth. The calculated stoichiometry for the $NaYF_4$ NCs, $Na_1Y_{0.6}Er_{0.02}Yb_{0.08}F_{3.2}$, is in fair agreement with the expected stoichiometry of $Na_1Y_{0.8}Er_{0.02}Yb_{0.18}F_4$.

Figure S1c,d (SI) shows that the NCs have a hexagonal crystal structure (JCPDS No. 00-028-1192, cyan lines), as expected. Using the Scherrer equation,[37] a rough estimate of the core crystallite size can be calculated, which is ∼18 and 17 nm for the $NaYF_4$ and $NaYF_4$@SiO_2 NCs, respectively. For the $NaYF_4$@SiO_2 NCs, an extra broad band is present centered at a diffraction angle of ∼28°, which is due to the amorphous silica.

By combining the data from TEM and EDX, it was shown that $NaYF_4$ NCs doped with Er and Yb can be synthesized. The crystallite size from XRD and the NP size from TEM match very closely, indicating monocrystalline core NCs. Furthermore, silica overgrowth results in monodisperse $NaYF_4$@SiO_2 NCs in which the size, shape, and crystal phase of the core NCs are unaltered.

LUMINESCENCE PROPERTIES

To investigate the luminescence properties of the NCs, room-temperature emission and decay measurements were performed, as shown in Figure 2. All measurements were

DOI: 10.1021/acs.jpcc.6b10279
J. Phys. Chem. C 2017, 121, 3503−3510

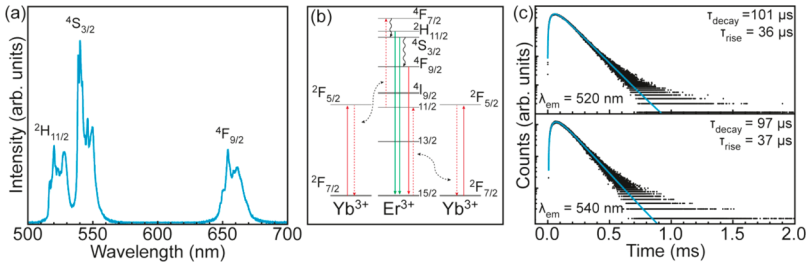

Figure 2. Emission spectrum of $NaYF_4$ NCs between 500 and 700 nm while exciting Yb^{3+} at 980 nm (a). Energy diagrams of Er^{3+} and Yb^{3+}, including the transitions involved in the UC process (b). Time-resolved luminescence measurements of emission from the $^2H_{11/2}$ (520 nm) and $^4S_{3/2}$ (545 nm) excited states upon excitation at 980 nm (c).

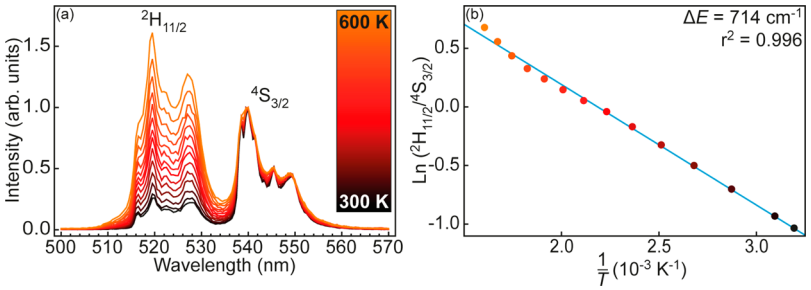

Figure 3. Emission spectra of $NaYF_4$ NCs upon excitation at 980 nm for temperatures ranging from 300 to 600 K recorded with steps of 25 K (a). The linear relation between the natural logarithm of the integrated intensity ratio of the $^2H_{11/2}$ and $^4S_{3/2}$ peak vs $1/T$ (b). The r^2 value for the fit, 0.996, is close to unity, and the steepness of the fit corresponds to a ΔE of 714 cm^{-1}. Five spectra were measured at every temperature interval to estimate the error in the measurements; this error is within the dot size of the data points.

performed using continuous-wave and pulsed lasers at 980 nm for the emission and decay measurements, respectively.

Figure 2a shows the upconversion (UC) emission spectrum upon excitation of Yb^{3+} at 980 nm. In the region between 500 and 700 nm, three distinct peaks are observed, centered around 525, 545, and 660 nm. These peaks correspond to the $^2H_{11/2}$–$^4I_{15/2}$, $^4S_{3/2}$–$^4I_{15/2}$, and $^4F_{9/2}$–$^4I_{15/2}$ transitions of Er^{3+}, respectively, as shown in Figure 2b.

Figure 2c depicts the luminescence lifetime measurements of the $^2H_{11/2}$ (top) and $^4S_{3/2}$ (bottom) excited state. The experimental data are shown in black, while a biexponential fit is shown in cyan. In both cases, a rise and a subsequent decay in luminescence is observed. The rise times are ∼35 μs and can be explained by the UC energy transfer from Yb^{3+} to Er^{3+}. The decay time of ∼100 μs is determined by both radiative decay to all lower levels and nonradiative relaxation to the $^4F_{9/2}$ level of Er^{3+}, in agreement with earlier reports.[38] The luminescence decay curves of the $^2H_{11/2}$ (λ_{em} = 520 nm) and $^4S_{3/2}$ (λ_{em} = 540 nm) excited states are nearly identical, which is expected for excited states that are thermally coupled.

FLUORESCENCE INTENSITY RATIO NANOTHERMOMETRY

FIR nanothermometry with luminescent nanoparticles relies on measuring the intensity ratio of emission lines from thermally coupled excited states. The population ratio of two excited states is determined by a Boltzmann distribution, which includes a temperature-dependent factor, as shown in eq 1.

$$\frac{N_2}{N_1} = e^{-\Delta E/kT} \tag{1}$$

Here, ΔE is the energy difference between the two excited states, k is the Boltzmann constant, and N_i is the population of state i. Emission intensities scale linearly with the population of an emitting state. This results in a temperature dependence of the luminescence intensity ratio, as shown in eq 2.

$$\frac{I_2}{I_1} = \frac{g_2 A_2 h\nu_2 N_2}{g_1 A_1 h\nu_1 N_1} = Ce^{-\Delta E/kT} \tag{2}$$

Here, I_i, g_i, A_i, and ν_i are the (integrated) emission intensity, the degeneracy of the emitting level, the spontaneous emission rate, and the frequency of the transition from state i to the ground state. For Er^{3+} in $NaYF_4$ NCs, the energy difference between the $^2H_{11/2}$ and $^4S_{3/2}$ excited states is ∼711 cm^{-1}, as calculated from the spectrum in Figure 2a (using Eq S1, SI).

To investigate the NCs as temperature probes, temperature-dependent luminescence measurements were performed on powders of NCs at temperatures ranging from 300 to 600 K with intervals of 25 K. Each temperature interval consisted of 1 min of heating, followed by a dwell time of at least 15 min before measuring spectra to ensure that the sample temperature was the same as that recorded by the thermocouple in the heating stage. Furthermore, the thermocouple allows for monitoring and compensation of heating effects due to the laser heating.

Figure 3a shows spectra recorded from 300 (black) up to 600 K (orange). The spectra are normalized to the maximum intensity of the $^4S_{3/2}$–$^4I_{15/2}$ emission peak. Upon excitation at 980 nm, the characteristic luminescence peaks from the $^2H_{11/2}$–$^4I_{15/2}$ and the $^4S_{3/2}$–$^4I_{15/2}$ transitions can be observed at all temperatures. The energy difference between these peaks is calculated to be 710 cm^{-1}. The intensity ratio between these peaks changes with increasing temperature, as expected for thermally coupled excited states.

To evaluate the temperature-dependent luminescence further, the natural logarithm of the integrated intensity ratio is plotted versus $1/T$, as shown in Figure 3b. The data points can be fitted with a linear fit, as expected from eq 2. The quality

DOI: 10.1021/acs.jpcc.6b10279
J. Phys. Chem. C 2017, 121, 3503−3510

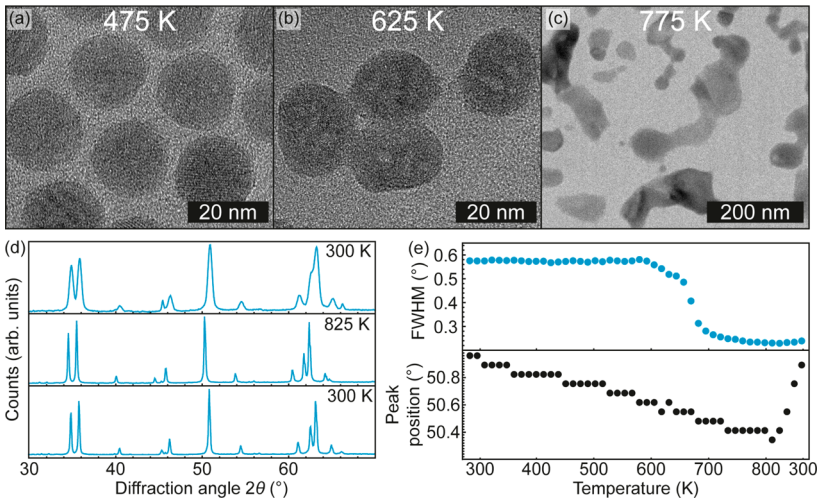

Figure 4. In situ TEM micrographs of $NaYF_4$ NCs at 475, 625, and 775 K (a–c, respectively). In situ XRD diffractograms (d) of $NaYF_4$ NCs before heating, during heating, and after heating to 825 K (top, middle, and bottom, respectively) and the corresponding fwhm and peak position of the (201) diffraction peak at 51° vs temperature (e).

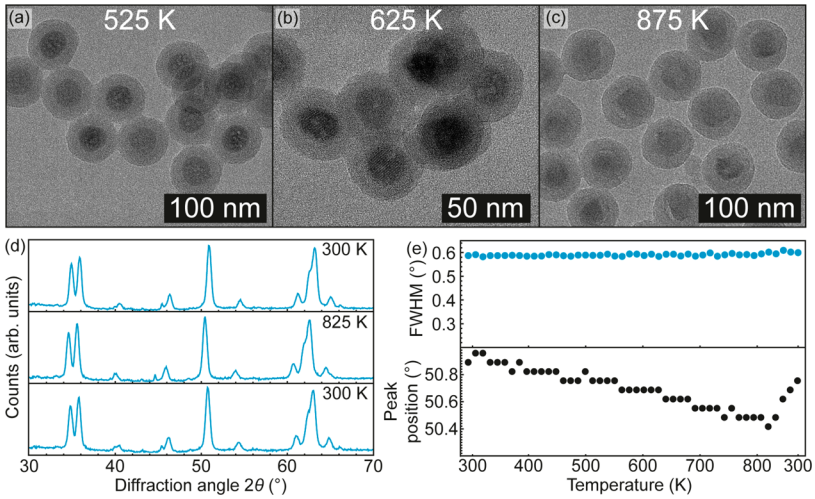

Figure 5. In situ TEM micrographs of $NaYF_4$@SiO_2 NCs at 525, 625, and 875 K (a–c, respectively). In situ XRD diffractograms (d) of $NaYF_4$@SiO_2 NCs before heating, during heating, and after heating to 825 K (top, middle, and bottom, respectively) and the corresponding fwhm and peak position of the diffraction peak at 51° vs temperature (e).

of this fit is high, as shown by the r^2 value of 0.996. From the slope of the linear fit, the energy difference between the excited states, ΔE, is calculated to be 714 cm^{-1} in these NCs. This calculated ΔE closely matches the experimental values of ΔE of 711 and 710 cm^{-1} determined from Figures 2a and 3a, respectively.

Using the relation between the temperature and luminescence intensity ratio of the $^4S_{3/2}$ and the $^2H_{11/2}$ peaks in Figure 3, it is evident that these NCs can be used as temperature probes from 300 to 600 K. At higher temperatures, the overall luminescence intensity dropped, and it was too low to determine temperatures accurately. The intensity drop above 600 K was accompanied by a brown discoloration of the NC powders. The discoloration is most likely due to the oxidation of the organic ligands capping the NCs. Due to this decrease in luminescence intensity, the NCs could not be used above 600 K for temperature sensing.

IN SITU STRUCTURAL CHARACTERIZATION

In situ TEM and XRD measurements were performed in order to investigate the origin of the sudden drop in luminescence intensity above 600 K. TEM micrographs were taken in situ while heating the NCs that were drop-casted on a special TEM heating chip with intervals of 50 K up to 875 K. XRD measurements, taking ~12 min for one XRD pattern, were performed continuously while heating the sample to 825 K in 9 h and afterward cooling down in 45 min.

Figure 4 shows the resulting TEM images of core NCs at 475, 625, and 775 K (panels a–c, respectively). Figure 4d shows three diffractograms taken before heating, during heating, and after heating (top, middle, and bottom, respectively). The fwhm and peak position of the (201) diffraction peak at 51° were extracted from all diffractograms and plotted versus temperature, as shown in Figure 4e (top and bottom, respectively).

Up to 575 K, individual NCs can be observed in the TEM images. However, upon further heating, particles start to coalesce and subsequently melt together completely, forming

DOI: 10.1021/acs.jpcc.6b10279
J. Phys. Chem. C 2017, 121, 3503–3510

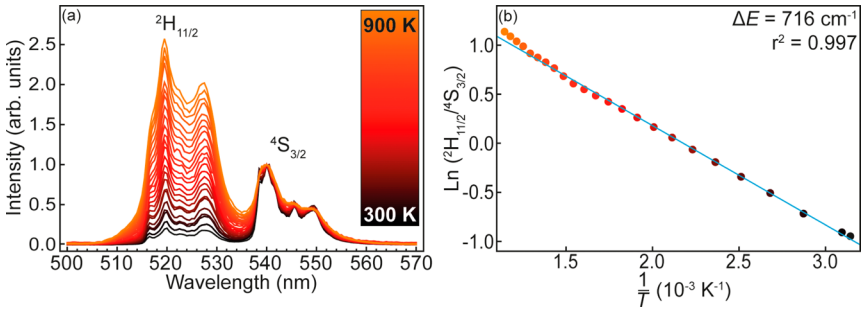

Figure 6. Emission spectra of $NaYF_4$@SiO_2 NCs upon excitation at 980 nm taken at temperatures ranging from 300 to 900 K with steps of 25 K (a). The linear relation between the natural logarithm of the integrated intensity ratio of the $^2H_{11/2}$ and $^4S_{3/2}$ peak is plotted vs $1/T$ (b). The r^2 value for the fit, 0.997, is close to unity, and the steepness of the fit corresponds to a ΔE of 716 cm^{-1}. Five spectra were measured at every temperature interval to estimate the error in the measurements; this error is within the dot size of the data points.

large clusters of material. The temperature at which the coalescence starts, that is, 625 K, matches the temperature at which the decrease in luminescence starts to occur. The XRD diffractograms show the characteristic peaks of hexagonal $NaYF_4$ shifting slightly upon heating due to thermal expansion of the crystal lattice. No phase transitions are observed, which is in accordance with investigations of Mathews and co-workers.[39] However, the diffraction peaks become irreversibly sharper at around 625 K. The fwhm decreases from 0.6 to 0.2°, corresponding to an increase in crystallite size. To summarize, the results show that the NCs coalesce, starting at temperatures around 625 K.

The temperature at which the luminescence intensity decreases dramatically corresponds to the temperature at which the NCs start to coalesce, as confirmed with TEM and XRD. It is likely that the atomic alignment of the NCs during coalescence/sintering is imperfect, resulting in the introduction of defects in the crystals. These defects can act as quenching sites for luminescence and therefore explain the sudden decrease in luminescence intensity in addition to the ligand oxidation discussed above.

The same in situ measurements were performed on the $NaYF_4$@SiO_2 NCs, as shown in Figure 5. In contrast to the $NaYF_4$ NCs, the $NaYF_4$@SiO_2 NCs remain well separated on the TEM images for all temperatures, showing that no interparticle alloying or intraparticle coalescence occurs. The fwhm of the (201) diffraction peak at 51° is constant during the entire thermal cycle, suggesting that the crystallite size remains unaltered. The overgrowth with silica, resulting in the core/shell architecture, ensures that the NCs are thermally stable up to 875 K and show no luminescence quenching up to at least 900 K.

(TEMPERATURE-DEPENDENT) PHOTOLUMINESCENCE OF $NAYF_4$@SIO_2 NANOCRYSTALS

To improve the temperature stability and thus extend the temperature range for nanothermometry, the $NaYF_4$ NCs were coated with a protective silica shell. The SiO_2 shell replaces the organic ligands and can prevent luminescence quenching due to oxidation of ligands and NCs coalescence. To investigate if the silica overgrowth has an effect on the luminescence properties of the NC cores, (time-resolved) room-temperature luminescence measurements were performed similar to those shown in Figure 2. The results, included in Figure S2, reveal that the emission spectra are nearly identical except for a small increase in the relative intensity of the $^4F_{9/2}$–$^4I_{15/2}$ emission. Also, the decay time of the $^4S_{3/2}$ and $^2H_{11/2}$ excited states are slightly shorter (85 μs after silica overgrowth vs 100 μs before). The shortening of the lifetime suggests that nonradiative relaxation to lower-lying $^4F_{9/2}$ states has increased, which is consistent with the observed increase in relative intensity of the $^4F_{9/2}$–$^4I_{15/2}$ emission. The increase of nonradiative relaxation can be explained by the presence of hydroxyl groups in the silica shell.[40,41] These hydroxyl groups are present because of incomplete condensation of neighboring silanol groups, Si–OH. These silanol groups condense to form typical Si–O–Si bonds in silica. The high-energy O–H vibration (ca. 3500 cm^{-1}) gives rise to faster multiphonon relaxation.

Although the additional O–H vibrations gives rise to faster decay times as a result of multiphonon relaxation, the energy levels of Er^{3+} remain unaltered due to shielding of the f orbitals. The unaltered energy levels dictate that the energy difference, ΔE, between the $^2H_{11/2}$ and $^4S_{3/2}$ state, and therefore the temperature-dependent luminescence, is not expected to change, which is in agreement with the experimental results.

In order to investigate the temperature-dependent luminescence properties of the silica-coated NCs, emission spectra were measured at different temperatures under 980 nm excitation. Figure 6a shows the spectra taken from 300 (black) up to 900 K (orange), normalized to the maximum intensity of the $^4S_{3/2}$–$^4I_{15/2}$ emission peak. The characteristic luminescence peaks from the $^2H_{11/2}$–$^4I_{15/2}$ and the $^4S_{3/2}$–$^4I_{15/2}$ transitions can be observed up to 900 K!

There is a small decrease in intensity, but clearly the temperature stability of the emission is strongly improved in comparison to the $NaYF_4$ cores. At the temperature limit of our experimental setup (900 K), the emission spectra are still well-resolved, suggesting that significantly higher temperatures can be probed. The emission intensity and signal-to-noise ratio hardly change between room temperature and 900 K. As can be observed in Figure 6a, the signal-to-noise ratio remains high up to the highest temperatures. The temperature limit of 900 K is solely set by the limitations of our instrumentation.

To calibrate the silica-coated NCs as a temperature probe, the natural logarithm of the integrated intensity ratio is plotted versus $1/T$, as shown in Figure 6b. The data points can be fitted with a linear fit, similar to Figure 3b.

The quality of the fit is high, as shown by the r^2 value of 0.997. From the slope of the linear fit, the energy difference between the excited states, ΔE, can be calculated to be 716 cm^{-1} and closely matches the experimental value of ΔE determined from the spectra and from the temperature-dependent emission spectra of the $NaYF_4$ core particles. The

DOI: 10.1021/acs.jpcc.6b10279
J. Phys. Chem. C 2017, 121, 3503–3510

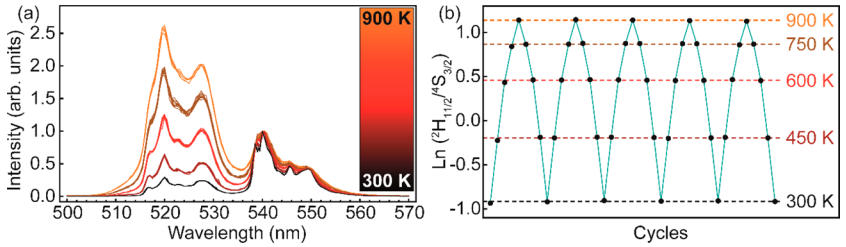

Figure 7. Emission spectra of $NaYF_4$@SiO_2 upon excitation at 980 nm while cycling the temperature between 300, 450, 600, 750, and 900 K five times (a). The natural logarithm of the fluorescence intensity ratio plotted per cycle step (black dots). The cyan line is to direct the eyes, and the dashed lines are the means of the data points per temperature (b).

results show that the maximum temperature range of the core particles can be expanded up to at least 900 K by applying a protective silica shell. The linear fit shows good agreement with the data points over the full temperature range.

THERMAL CYCLING EXPERIMENT

In addition to having high thermal stability and temperature accuracy, it is important that a temperature sensor can survive multiple thermal cycles without a change in properties. To investigate the durability of the $NaYF_4$@SiO_2 NCs, the temperature probes were cycled between 300 and 900 K five times. During the heating up and cooling down in each cycle, luminescence measurements were performed at 300, 450, 600, 750, and 900 K.

Figure 7a shows the spectra taken at five different temperatures during the cycle experiment, normalized to the $^4S_{3/2}$–$^4I_{15/2}$ emission peak. The spectra at a specific temperature are very similar. At each temperature, the intensity ratio of the two emission peaks was determined and is plotted in Figure 7b. The data points (black) follow identical trends during the five cycles (cyan line). The average fluorescence intensity ratios for each temperature were calculated from the data (dashed lines). The data points only have small deviations from the average. The thermal cycling experiment shows that the temperature probes are stable and durable up to 900 K.

The standard deviations in temperature are calculated to be 1.1, 1.8, 2.9, 5.2, and 5.3 K for 300, 450, 600, 750, and 900 K, respectively. These values are high compared to the very accurate temperature probes used for bioimaging (<0.5 K[15]). Temperature accuracies down to 0.2 or 0.3 K have been reported for the Yb–Er and Yb–Tm couple in the biologically interesting temperature window.[42−45] The smaller standard deviations for temperature measurements in bioimaging are expected based on the smaller temperature range. The probes used are optimized for this temperature range such that the change in intensity ratio with temperature is large.

In the case of FIRT, also the sensitivity S and relative sensitivity of a temperature probe are often used as a quality measure of the performance as a temperature sensor. S is defined as the change of the intensity ratio R with temperature, as shown in eq 3.

$$S = \frac{dR}{dT} \tag{3}$$

The relative sensitivity is defined as S/R (in % K^{-1}). For a large temperature range, the change in the intensity ratio with temperature varies with temperature, and thus, the relative sensitivity will be different in different temperature regimes. For the $NaYF_4$:Er,Yb nanoparticles in the 300–900 K temperature range, the sensitivity, calculated using eqs 2 and 3 (with C = 9.4), shows that the relative sensitivity decreases from 1.02% K^{-1} at 300 K to 0.13% K^{-1} at 900 K. The 1.02% K^{-1} sensitivity is consistent with values typically found at around 300 K for Er^{3+} (between 0.5 and 1.5% K^{-1}).[46] The variation in relative sensitivity with temperature is inherent to using temperature probes in a wide range. The sensitivity of a temperature probe cannot be optimized for the full temperature window. Most applications that require a broader temperature sensing range do not require a sensitivity of 0.5 K. However, care should be taken that the error in the temperature measurement does not become too large. In our case, a measurement error of ∼5 at 900 K is sufficient for most applications.

The present results demonstrate for the first time the use of ∼50 nm NCs for high-temperature nanothermometry using a silica coating to stabilize the NCs. Silica-stabilized NCs of other host materials (e.g., oxides) and also other Ln^{3+} dopants with a different ΔE between levels can be developed to realize other high-temperature nanoprobes with potentially higher sensitivity in the high-temperature range.[47]

In summary, we have reported $NaYF_4$:Er^{3+},Yb^{3+} NCs coated with a SiO_2 shell as stable nanoprobes for high-temperature nanothermometry, up to 900 K. The temperature-dependent intensity ratio of emission from the $^2H_{11/2}$ level (520 nm) and the $^4S_{3/2}$ level (545 nm) follows a Boltzmann distribution. From the intensity ratio, temperatures can be measured accurately (1–5 K accuracy) using remote sensing techniques. The temperature stability of the probes is confirmed by in situ TEM and XRD. The temperature-dependent luminescence remains unaltered in multiple cycling experiments between 300 and 900 K. On the basis of these observations, the $NaYF_4$:Er^{3+},Yb^{3+} nanoprobes provide a noninvasive temperature probe that is dispersible in liquids and has a broad range for temperature sensing. It can therefore be used for high-resolution temperature sensing in a wide range of applications, including chemical reactors and nanoelectronics. The reported method of strongly improving the thermal stability of nanoprobes by silica coating can be generally applied to enhance the performance of other nanoprobes.

ASSOCIATED CONTENT

Supporting Information

The Supporting Information is available free of charge on the ACS Publications website at DOI: 10.1021/acs.jpcc.6b10279.

Experimental methods: EDX and ex situ XRD data for both $NaYF_4$ and $NaYF_4$@SiO_2 (Figure S1) and (time-resolved) luminescence measurements of the $NaYF_4$@SiO_2 NCs (Figure S2) (PDF)

DOI: 10.1021/acs.jpcc.6b10279
J. Phys. Chem. C 2017, 121, 3503−3510

AUTHOR INFORMATION

Corresponding Author

*E-mail: R.G.Geitenbeek@uu.nl.

ORCID

Bert M. Weckhuysen: 0000-0001-5245-1426

Andries Meijerink: 0000-0003-3573-9289

Notes

The authors declare no competing financial interest.

ACKNOWLEDGMENTS

The authors acknowledge the assistance of J. Meeldijk and M. Versluijs-Helder, both from Utrecht University, with TEM and XRD measurements, respectively. This work was supported by the Netherlands Center for Multiscale Catalytic Energy Conversion (MCEC), an NWO Gravitation programme funded by the Ministry of Education, Culture and Science of the government of The Netherlands. The authors acknowledge financial support from the European Research Council under the European Unions Seventh Framework Programme (FP-2007-2013)/ERC Advanced Grant Agreement 291667 HierarSACol.

REFERENCES

(1) Kim, T.-H.; Cho, K.-S.; Lee, E. K.; Lee, S. J.; Chae, J.; Kim, J. W.; Kim, D. H.; Kwon, J.-Y.; Amaratunga, G.; Lee, S. Y.; et al. Full-Colour Quantum Dot Displays Fabricated by Transfer Printing. *Nat. Photonics* **2011**, *5*, 176−182.

(2) Jang, E.; Jun, S.; Jang, H.; Lim, J.; Kim, B.; Kim, Y. White-Light-Emitting Diodes with Quantum Dot Color Converters for Display Backlights. *Adv. Mater.* **2010**, *22*, 3076−3080.

(3) Lim, S. F.; Riehn, R.; Ryu, W. S.; Khanarian, N.; Tung, C.-k.; Tank, D.; Austin, R. H. *In Vivo* and Scanning Electron Microscopy Imaging of Upconverting Nanophosphors in Caenorhabditis elegans. *Nano Lett.* **2006**, *6*, 169−174.

(4) Zrazhevskiy, P.; Sena, M.; Gao, X. Designing Multifunctional Quantum Dots for Bioimaging, Detection, and Drug Delivery. *Chem. Soc. Rev.* **2010**, *39*, 4326−4354.

(5) van der Ende, B. M.; Aarts, L.; Meijerink, A. Lanthanide Ions as Spectral Converters for Solar Cells. *Phys. Chem. Chem. Phys.* **2009**, *11*, 11081−11095.

(6) Chuang, C.-h. M.; Brown, P. R.; Bulović, V.; Bawendi, M. G. Improved Performance and Stability in Quantum Dot Solar Cells through Band Alignment Engineering. *Nat. Mater.* **2014**, *13*, 796−801.

(7) Zhang, Y.; Tang, Z.-R.; Fu, X.; Xu, Y.-J. TiO_2-Graphene Nanocomposites for Gas-Phase Photocatalytic Degradation of Volatile Aromatic Pollutant: Is TiO_2-Graphene Truly Different from Other TiO_2-Carbon Composite Materials? *ACS Nano* **2010**, *4*, 7303−7314.

(8) Bezemer, G. L.; Bitter, J. H.; Kuipers, H. P. C. E.; Oosterbeek, H.; Holewijn, J. E.; Xu, X.; Kapteijn, F.; Van Dillen, A. J.; De Jong, K. P. Cobalt Particle Size Effects in the Fischer−Tropsch Reaction Studied with Carbon Nanofiber Supported Catalysts. *J. Am. Chem. Soc.* **2006**, *128*, 3956−3964.

(9) Mecklenburg, M.; Hubbard, W. A.; White, E. R.; Dhall, R.; Cronin, S. B.; Aloni, S.; Regan, B. C. Nanoscale Temperature Mapping in Operating Microelectronic Devices. *Science* **2015**, *347*, 629−633.

(10) Kim, K.; Chung, J.; Hwang, G.; Kwon, O.; Lee, J. S. Quantitative Measurement with Scanning Thermal Microscope by Preventing the Distortion due to the Heat Transfer through the Air. *ACS Nano* **2011**, *5*, 8700−8709.

(11) Smith, J. D.; Cappa, C. D.; Drisdell, W. S.; Cohen, R. C.; Saykally, R. J. Raman Thermometry Measurements of Free Evaporation from Liquid Water Droplets. *J. Am. Chem. Soc.* **2006**, *128*, 12892−12898.

(12) Quintanilla, M.; Cantelar, E.; Cussó, F.; Villegas, M.; Caballero, A. C. Temperature Sensing with Up-Converting Submicron-Sized $LiNbO_3$:Er^{3+}/Yb^{3+} Particles. *Appl. Phys. Express* **2011**, *4*, 022601.

(13) Brites, C. D. S.; Lima, P. P.; Silva, N. J. O.; Millán, A.; Amaral, V. S.; Palacio, F.; Carlos, L. D. Thermometry at the Nanoscale. *Nanoscale* **2012**, *4*, 4799−4829.

(14) Jaque, D.; Vetrone, F. Luminescence Nanothermometry. *Nanoscale* **2012**, *4*, 4301−4326.

(15) Gota, C.; Okabe, K.; Funatsu, T.; Harada, Y.; Uchiyama, S. Hydrophilic Fluorescent Nanogel Thermometer for Intracellular Thermometry. *J. Am. Chem. Soc.* **2009**, *131*, 2766−2767.

(16) Yang, J. M.; Yang, H.; Lin, L. Quantum Dot Nano Thermometers Reveal Heterogeneous Local Thermogenesis in Living Cells. *ACS Nano* **2011**, *5*, 5067−5071.

(17) Vetrone, F.; Naccache, R.; Zamarrón, A.; Juarranz de la Fuente, A.; Sanz-Rodríguez, F.; Martinez Maestro, L.; Martín Rodriguez, E.; Jaque, D.; García Solé, J.; Capobianco, J. A. Temperature Sensing Using Fluorescent Nanothermometers. *ACS Nano* **2010**, *4*, 3254−3258.

(18) Bar-Cohen, A.; Wang, P. On-chip Hot Spot Remediation with Miniaturized Thermoelectric Coolers. *Microgravity Sci. Technol.* **2009**, *21*, 351−359.

(19) Aigouy, L.; Tessier, G.; Mortier, M.; Charlot, B. Scanning Thermal Imaging of Microelectronic Circuits with a Fluorescent Nanoprobe. *Appl. Phys. Lett.* **2005**, *87*, 184105/1−184105/3.

(20) Jundt, D. H. Temperature-Dependent Sellmeier Equation for the Index of Refraction, n_e, in Congruent Lithium Niobate. *Opt. Lett.* **1997**, *22*, 1553−1555.

(21) Romero, J. J.; Arago, C.; Gonzalo, J. A.; Jaque, D.; Garcia Sole, J. Spectral and Thermal Properties of Quasiphase-Matching Second-Harmonic-Generation in Nd^{3+}: $Sr_{0.6}Ba_{0.4}(NbO_3)_2$ Multiself-Frequency-Converter Nonlinear Crystals. *J. Appl. Phys.* **2003**, *93*, 3111−3113.

(22) Feuerstein, A.; Knapp, J.; Taylor, T.; Ashary, A.; Bolcavage, A.; Hitchman, N. Technical and Economical Aspects of Current Thermal Barrier Coating Systems for Gas Turbine Engines by Thermal Spray and EBPVD: A Review. *J. Therm. Spray Technol.* **2008**, *17*, 199−213.

(23) Vaβen, R.; Jarligo, M. O.; Steinke, T.; Mack, D. E.; Stöver, D. Overview on Advanced Thermal Barrier Coatings. *Surf. Coat. Technol.* **2010**, *205*, 938−942.

(24) Toebes, M.; Prinsloo, F. F.; Bitter, J. H.; van Dillen, A. J.; de Jong, K. P. Influence of Oxygen-Containing Surface Groups on the Activity and Selectivity of Carbon Nanofiber-Supported Ruthenium Catalysts in the Hydrogenation of Cinnamaldehyde. *J. Catal.* **2003**, *214*, 78−87.

(25) Borodina, E.; Meirer, F.; Lezcano-Gonzalez, I.; Mokhtar, M.; Asiri, A. M.; Al-Thabaiti, S. A.; Basahel, S. N.; Ruiz-Martinez, J.; Weckhuysen, B. M. Influence of the Reaction Temperature on the Nature of the Active and Deactivating Species during Methanol-to-Olefins Conversion over H-SSZ-13. *ACS Catal.* **2015**, *5*, 992−1003.

(26) Peng, H. S.; Huang, S. H.; Wolfbeis, O. S. Ratiometric Fluorescent Nanoparticles for Sensing Temperature. *J. Nanopart. Res.* **2010**, *12*, 2729−2733.

(27) Cui, Y.; Xu, H.; Yue, Y.; Guo, Z.; Yu, J.; Chen, Z.; Gao, J.; Yang, Y.; Qian, G.; Chen, B. A Luminescent Mixed-Lanthanide Metal-Organic Framework Thermometer. *J. Am. Chem. Soc.* **2012**, *134*, 3979−3982.

(28) Rai, V. K.; Rai, D.; Rai, S. Pr^{3+} Doped Lithium Tellurite Glass as a Temperature Sensor. *Sens. Actuators, A* **2006**, *128*, 14−17.

(29) Pandey, A.; Rai, V. K. Optical Thermometry using FIR of Two Close Lying Levels of Different Ions in Y_2O_3:Ho^{3+}-Tm^{3+}-Yb^{3+} phosphor. *Appl. Phys. B: Lasers Opt.* **2013**, *113*, 221−225.

(30) Blasse, G.; Grabmaier, B. *Luminescent Materials*; Springer: Berlin, Germany, 1994.

(31) Tripathi, G.; Rai, V. K.; Rai, S. Optical Properties of Sm^{3+}:CaO-Li_2O-B_2O_3-BaO Glass and Codoped Sm^{3+}:Eu^{3+}. *Appl. Phys. B: Lasers Opt.* **2006**, *84*, 459−464.

(32) Haro-González, P.; Martín, I.; Martín, L.; León-Luis, S. F.; Pérez-Rodríguez, C.; Lavín, V. Characterization of Er^{3+} and Nd^{3+} Doped Strontium Barium Niobate Glass Ceramic as Temperature Sensors. *Opt. Mater.* **2011**, *33*, 742−745.

DOI: 10.1021/acs.jpcc.6b10279
J. Phys. Chem. C 2017, 121, 3503−3510

(33) Singh, S. K.; Kumar, K.; Rai, S. Er^{3+}/Yb^{3+} Codoped Gd_2O_3 Nano-Phosphor for Optical Thermometry. *Sens. Actuators, A* **2009**, *149*, 16−20.
(34) Cao, B.; He, Y.; Feng, Z.; Li, Y.; Dong, B. Optical Temperature Sensing Behavior of Enhanced Green Upconversion Emissions from Er-Mo:$Yb_2Ti_2O_7$ Nanophosphor. *Sens. Actuators, B* **2011**, *159*, 8−11.
(35) Li, D.; Wang, Y.; Zhang, X.; Yang, K.; Liu, L.; Song, Y. Optical Temperature Sensor Through Infrared Excited Blue Upconversion Emission in Tm^{3+}/Yb^{3+} Codoped Y_2O_3. *Opt. Commun.* **2012**, *285*, 1925−1928.
(36) Padture, N. P.; Gell, M.; Jordan, E. H. Thermal Barrier Coatings for Gas-Turbine Engine Applications. *Science* **2002**, *296*, 280−284.
(37) Scherrer, P. Bestimmung der Größe und der Inneren Struktur von Kolloidteilchen mittels Röntgenstrahlen. *Nachr. Ges. Wiss. Goettingen* **1918**, *1918*, 98−100.
(38) Suyver, J. F.; Grimm, J.; Van Veen, M. K.; Biner, D.; Krämer, K. W.; Güdel, H. U. Upconversion Spectroscopy and Properties of $NaYF_4$ Doped with Er^{3+}, Tm^{3+} and/or Yb^{3+}. *J. Lumin.* **2006**, *117*, 1−12.
(39) Mathews, M.; Ambekar, B.; Tyagi, A.; Köhler, J. High Temperature X-ray Diffraction Studies on Sodium Yttrium Fluoride. *J. Alloys Compd.* **2004**, *377*, 162−166.
(40) van Blaaderen, A.; Kentgens, A. Particle Morphology and Chemical Microstructure of Colloidal Silica Spheres Made from Alkoxysilanes. *J. Non-Cryst. Solids* **1992**, *149*, 161−178.
(41) Zhang, L.; D'Acunzi, M.; Kappl, M.; Imhof, A.; van Blaaderen, A.; Butt, H.-J.; Graf, R.; Vollmer, D. Tuning the Mechanical Properties of Silica Microcapsules. *Phys. Chem. Chem. Phys.* **2010**, *12*, 15392−15398.
(42) dos Santos, P. V.; de Araujo, M. T.; Gouveia-Neto, A. S.; Neto, J. A. M.; Sombra, S. B. Optical Thermometry Through Infrared Excited Upconversion Fluorescence Emission in Er^{3+} and Er^{3+}-Yb^{3+}-doped Chalcogenide Glasses. *IEEE J. Quantum Electron.* **1999**, *35*, 395−399.
(43) Li, C. R.; Dong, B.; Ming, C. G.; Lei, M. Application to Temperature Sensor Based on Green Up-Conversion of Er3+ Doped Silicate Glass. *Sensors* **2007**, *7*, 2652−2659.
(44) Dong, N.-N.; Pedroni, M.; Piccinelli, F.; Conti, G.; Sbarbati, A.; Ramírez-Hernandez, J. E.; Maestro, L. M.; Iglesias-de la Cruz, M. C.; Sanz-Rodriguez, F.; Juarranz, A.; Chen, F.; Vetrone, F.; Capobianco, J. A.; Sole, J. G.; Bettinelli, M.; Jaque, D.; Speghini, A. NIR-to-NIR Two-Photon Excited CaF_2:Tm^{3+},Yb^{3+} Nanoparticles: Multifunctional Nanoprobes for Highly Penetrating Fluorescence Bio-Imaging. *ACS Nano* **2011**, *5*, 8665−8671.
(45) Li, C. R.; Dong, B.; Li, S. F.; Song, C. Er^{3+}-Yb^{3+} Co-Doped Silicate Glass for Optical Temperature Sensor. *Chem. Phys. Lett.* **2007**, *443*, 426−429.
(46) Debasu, M. L.; Ananias, D.; Pastoriza-Santos, I.; Liz-Marzán, L. M.; Rocha, J.; Carlos, L. D. All-In-One Optical Heater-Thermometer Nanoplatform Operative From 300 to 2000 K Based on Er^{3+} Emission and Blackbody Radiation. *Adv. Mater.* **2013**, *25*, 4868−4874.
(47) Dong, B.; Cao, B.; He, Y.; Liu, Z.; Li, Z.; Feng, Z. Temperature Sensing and In Vivo Imaging by Molybdenum Sensitized Visible Upconversion Luminescence of Rare-Earth Oxides. *Adv. Mater.* **2012**, *24*, 1987−1993.

DOI: 10.1021/acs.jpcc.6b10279
J. Phys. Chem. C 2017, 121, 3503−3510